IEEE Access
Multidisciplinary | Rapid Review | Open Access Journal

Received June 3, 2020, accepted June 25, 2020, date of publication June 30, 2020, date of current version July 20, 2020.

Digital Object Identifier 10.1109/ACCESS.2020.3006062

Detection and Parameter Estimation of Solitary Internal Waves Using Distributed Acoustic Sensors

TONGCHEN WANG, T. C. YANG, AND WEN XU, (Senior Member, IEEE)
College of Information Science and Electronic Engineering, Zhejiang University, Hangzhou 310027, China
Zhejiang Provincial Key Laboratory of Ocean Observation-Imaging Testbed, Zhoushan 316021, China

Corresponding author: T. C. Yang (tcyang@zju.edu.cn)

This work was supported by the Natural Science Foundation of China under Grant 61531017 and Grant 61831020.

ABSTRACT A method to detect solitary internal waves passing through the sensors area in shallow water and estimate their parameters is proposed in this paper using distributed acoustic sensors. The proposed detection method is based on cross correlation of the (envelop of) channel impulse responses estimated from broadband signals transmitted between the sensor nodes with the reference impulse responses in the absence of solitary internal waves. An iterative sequential parameter estimation method is proposed based on time domain matching of the measured channel impulse responses with modeled impulse responses. Simultaneous parameter estimation can be obtained using a global search method such as the matched field inversion. Simulation studies are carried out using environmental acoustic data collected in the northern South China Sea. The results show that the proposed method can effectively detect the existence of passing SIWs, and their parameters can be estimated with reasonable accuracy even under low signal-to-noise ratio conditions.

INDEX TERMS Solitary internal waves, detection, parameter estimations.

I. INTRODUCTION

Nonlinear internal waves, also known as solitary internal waves (SIWs), are widely found in the continental shelf area around the world [1]. As SIWs move toward the coast, they change the sound speed profile (SSP) in both depth and range, and significantly impact sound propagation [2]. At the same time, sudden changes in ocean density and current provoked by SIWs may pose serious threats to the safe operation of oil rigs and underwater vehicles [3]. Therefore, it is of practical importance to develop effective detection and observation methods of SIWs and study their properties.

With the advances in ocean information acquisition techniques, observation methods of SIWs have been developed rapidly in recent years. In 1953, Shand introduced the remote sensing technique for observing the SIWs [4]; in 1985, Alpers proposed imaging of SIWs using synthetic aperture radar [5]. Currently, SIWs positions are mainly monitored by remote sensing. Sound speed changes caused by SIWs have been routinely measured by thermistor strings in oceanographic and acoustic experiments, which record the temperature data. An eigenvector analysis for these changes was done by Qu *et al.*, in 2019 [6]. A world map of SIWs was reported based on in-situ sensors, aircraft and satellites [1].

Although the satellite imaging method contributes much to the observation and study of SIWs, the data are limited by the satellite trajectory and weather conditions. In comparison, thermistor (temperature) data are spot measurements, and usually do not cover a wide area, thus providing limited information on the spatial distribution of SIWs. It is envisioned that in the future, many inexpensive sensors will be available and be deployed in the ocean as distributed sensor networks. The acoustic data collected from the network contain information about the underwater acoustic channel, and can be used to detect the existence of SIWs and study their properties using inverse methods. To achieve this goal, it is essential to study the effect of SIWs on the acoustic signal propagation. The readers are referred to the literatures, including work done by Duda [7], [8], Headrick [9], [10], Yoo [11], and Yang [11], [12] *et al.*

In this paper, we develop inverse acoustic methods for detection and parameter estimation of SIWs. Specifically, we use acoustic data collected on the distributed sensors to: 1) determine when the SIWs pass by, thereby to predict their positions at later time, and 2) estimate the parameters of SIWs based on matched field inversion (MFI) methods. Here the

The associate editor coordinating the review of this manuscript and approving it for publication was Kan Liu.

sound speed perturbation caused by SIWs is modeled as a function of SIW parameters, such as position, direction of travel, characteristic width and depth of solitons, and separations between them. Owing to the pre-deployed underwater distributed sensor network, the proposed method has the ability for long-time continuous observations of SIWs under nearly all kinds of weather conditions, and can achieve large-range observations with enough nodes.

The acoustic inverse method requires a model for the SIWs in order to calculate/estimate the forward propagation acoustic field. In this paper, we assume the standard SIW model with a secant waveform [1], [12]. The SIW model can be modified given real data.

This paper is organized as follows. Modeling of physical properties and sound speed perturbation of SIWs is given in Section II, which also introduces overall design idea of SIW detection and parameter estimation. Aimed at future ocean experiments, data processing and performance analyses of the proposed method are conducted using simulated data in Section III, for which example environment and SIWs properties in the northern South China Sea (SCS) are taking into consideration. A brief summary is given in Section IV.

II. PROBLEM STATEMENT

A. SOUND SPEED PERTUBATION CAUSED BY SIWS

Although SIWs occurring in different continental shelf regions all around the world differ in intensity and spatial scales, they have similar properties and can be characterized by the standard model based on the Korteweg-de Vries (KdV) equation [1]. The displacement of a single SIW (soliton) is expressed as [1], [12]:

$$\eta\left(r,z,t\right)=\eta_0\,\mathrm{sech}^2\left[\frac{r-r_0\left(t\right)}{\Delta}\right]W\left(z\right), \tag{1}$$

where $\eta\left(r,z,t\right)$ denotes the displacement along depth dimension at time t, depth z, and horizontal position r, η_0 is the amplitude of the soliton, $r_0(t)$ and Δ denote the center and characteristic width of the soliton, respectively. $W(z)$ here represents the first mode depth-function of the internal waves, and sech$(\cdot)$ is the hyperbolic secant function.

The sound speed perturbation caused by one soliton depends on its displacement as well as the reference sound speed (denoted as c_0), and can be expressed as [12], [13]:

$$\frac{\delta c\left(r,z,t\right)}{c_0}=G\left(z\right)N^2\left(z\right)\eta\left(r,z,t\right), \tag{2}$$

where $\delta c(r,z,t)$ denotes the sound speed perturbation at time t and position (r,z), $G(z)$ is a smooth function of depth, and $N(z)$ is the Brust-Väisälä buoyancy frequency. By combining (1) and (2), one can find the relationship between physical properties of one soliton and corresponding sound speed perturbation as:

$$\delta c\left(r,z,t\right)=c_0\eta_0 H\left(z\right)\mathrm{sech}^2\left[\frac{r-r_0\left(t\right)}{\Delta}\right], \tag{3}$$

where $H\left(z\right)\equiv G(z)N^2(z)W(z)$.

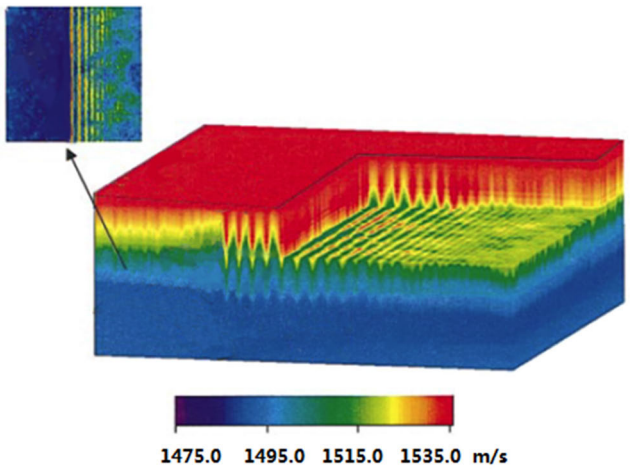

FIGURE 1. A sketch of the sound speed perturbation caused by SIWs in shallow water, repeated from Finette *et al.* in 2003 [15].[1]

SIWs can appear as a single soliton, a wave packet consisting of multiple solitons one following the other, and wave group composed of several wave packets. SIWs normally propagate in specific direction as plane waves or curved wave fronts and can have large displacement/amplitude (tens to hundreds of meters), and normally small range span (soliton width $\sim$ 500 m). The SIW waveforms (or parameters) may change with range (due to dispersion and change in water depth), but can be regarded as unchanged within a short propagation distance [14]. In a wave packet, the first soliton usually has the largest amplitude [11]–[14].

For a wave packet of SIWs, the sound speed perturbation is the superposition of sound speed perturbation caused by each soliton, as:

$$\delta c\left(r,z,t\right)=c_0H\left(z\right)\sum_i\eta_i\,\mathrm{sech}^2\left[\frac{r-r_i\left(t\right)}{\Delta_i}\right], \tag{4}$$

where the subscript i refers to the i-th solition. The sound speed model of SIWs in (4) will be incorporated in a numerical propagation model to calculate the acoustic field propagating through the SIWs.

B. ACOUSTIC METHOD FOR DETECTION OF SIWS

A 3-dimensional view of the SSP in the presence of a packet of solitons is shown in Fig. 1, repeated from Finette *et al.* in 2003 [15]. One observes that the change in sound speed is: 1) extensive in depth (determined by η_i), up to tens or even hundreds of meters in the real world, 2) anisotropic in horizontal distribution - thus its effect on sound propagation depends on the angle between the acoustic propagation and soliton wave front, and 3) changing with time as the SIWs move. Given (4), one can model the changes in the acoustic field propagating through SIWs, and based on that one can develop a detection method.

[1]Reprinted with permission from Horizontal array beamforming in an azimuthally anisotropic internal wave field. Copyright 2020, Acoustic Society of America.

The detection approach is designed basing on the dual-threshold detection method by selecting a pair of nodes from the distributed sensor network whose acoustic data are mostly sensitive to the passage of the SIWs. Since SIWs appear approximately semi-diurnally, acoustic data collected on sensors can be approximately seen as unchanged over a long period of time in the absence of SIWs. This data is set as the reference data, and can be updated adaptively by continuous measurement to account for slow changes in the background SSP. When the SIWs pass by the nodes, one expects to see drastic changes in the acoustic data which can be detected by correlating the received data with the reference data, as shown below in Sec. III. Two correlation methods are used: 1) correlation for received time series known as the Bartlett Processor [16],

$$Corr1 = \frac{|\mathbf{y}^H \mathbf{y}_0|^2}{||\mathbf{y}||^2 ||\mathbf{y}_0||^2}, \tag{5}$$

where $\mathbf{y}$ represents the measured acoustic data and $\mathbf{y}_0$ is the reference acoustic data; and 2) correlation of the data envelopes defined by

$$Corr2 = \frac{|\text{env}(\mathbf{y})^H \text{env}(\mathbf{y}_0)|^2}{||\text{env}(\mathbf{y})||^2 ||\text{env}(\mathbf{y}_0)||^2}, \tag{6}$$

where env$(\cdot)$ defines the data envelope and can be calculated by applying Hilbert Transform to the data then taking amplitudes. The correlation coefficients, (5) and (6), are normally high in the absence of SIWs. They drop to a low value when the SIWs enter the acoustic propagation plane. Thus, the arrival of SIWs can be detected by setting a reasonable threshold (the first threshold *ThrsL*), below which SIWs are declared as present.

The second threshold *ThrsT* is the ''number of consecutive measurements with low correlation'', which is used to distinguish SIWs passing through from other instantaneous perturbation of sound speed. Note that for a pair of nodes with fixed time interval of measurement, such as 1 minute, *ThrsT* represents processes of SIWs passing through, and the value of which should be chosen by considering the width and propagation speed of the SIWs, as discussed in Sec. III.

It has been learned that when the pair of nodes are more or less aligned with the wave fronts of the SIWs (see Fig. 1), the acoustic data will be more sensitive to SIW passing through due to the horizontal focusing/defocusing of the sound [17]. As the SIWs usually propagate toward the shore with a relatively known general direction which can be learned from previous satellites images, one can design the node topology to facilitate the detection of SIWs. See Sec. II.D for further discussions.

C. ACOUSTIC METHOD FOR PARAMETER ESTIMATION OF SIWS

The SIW parameters can be estimated from the received acoustic data using an inverse method assuming that SIWs have been detected. To simply the problem, we assume in this paper that the reference sound speed c_0 and buoyancy frequency or $H(z)$ in (4) are approximately known based on historical data, while other parameters of SIWs, like Δ_i, r_i, η_i, intervals between solitons L_i, and the exact propagation angle θ of a SIW are unknown and to be estimated from the acoustic data.

Equation (4) implies that the parameters of interest influence the sound speed perturbation $\delta c(r, z, t)$ simultaneously, and the sound speed perturbation is ''range-dependent''. As a result, one can use, for example, the MFI [16] method to estimate the SIW parameters from acoustic data received. The acoustic data $\mathbf{y}$ is theoretically described by

$$\mathbf{y} = s(f)\boldsymbol{h}(\mathbf{x}) + \mathbf{n}, \tag{7}$$

where $\boldsymbol{h}(\mathbf{x})$ denotes the channel transfer function, which is a vector function of $\mathbf{x} = [r_i, \Delta_i, \eta_i, L_i, \theta]$ for the i-th soliton, $s(f)$ denotes the source level at frequency f, and $\mathbf{n}$ is the noise. One can obtain the estimation value $\hat{\mathbf{x}}$ of $\mathbf{x}$ by finding the maximum value of the cost function B:

$$B = \frac{|\mathbf{y}^H \boldsymbol{h}(\bar{\mathbf{x}})|^2}{||\mathbf{y}||^2 ||\boldsymbol{h}(\bar{\mathbf{x}})||^2}, \tag{8}$$

where $\bar{\mathbf{x}}$ represents possible values of $\mathbf{x}$. Here the value of B are also calculated using normalized Bartlett Processor, as shown in (8), in which $\boldsymbol{h}(\cdot)$ need to be calculated using a (numerical) propagation model based on the sound speed given by (4). The maximum value of B can be searched by exhaustive calculations, or using optimization algorithms such as the genetic algorithm. Given measurements of r_i, one can estimate the velocity v, taking into account of the correction due to the propagation angle θ, as discussed in Sec. III.D.

Besides, for actual parameter estimation processes, certain parameters of the solitons, such as r_i, Δ_i, and η_i, can be measured for individual solitons one by one using acoustic data measured from node pairs in small meshes. After that, L_i can be estimated by using data from node pairs with longer spacing (referring to Fig. 2). Here the detection results of SIWs can be used to map solitons into node meshes of the distributed sensor network. More details are shown in numerical analyses for the proposed method in Sec. III.D.

D. NODE DEPLOYMENT

Proper placements of sensor nodes (in a distributed sensor network) could have a significant impact on the performance of the proposed method for SIW detection and parameter estimation. In a shallow water environment, sensor nodes are designed to be deployed on the sea bed instead of suspending in water column, in view of the following: 1) Changes of sound speed due to seawater temperature, tides, *et al.* are smaller in lower part of the water body. 2) Nodes, once deployed, will not move with waves, which can reduce measurement error of acoustic data. This choice is reasonable if the sound speed perturbation caused by the SIWs affect a significant portion of the water column, so that the acoustic

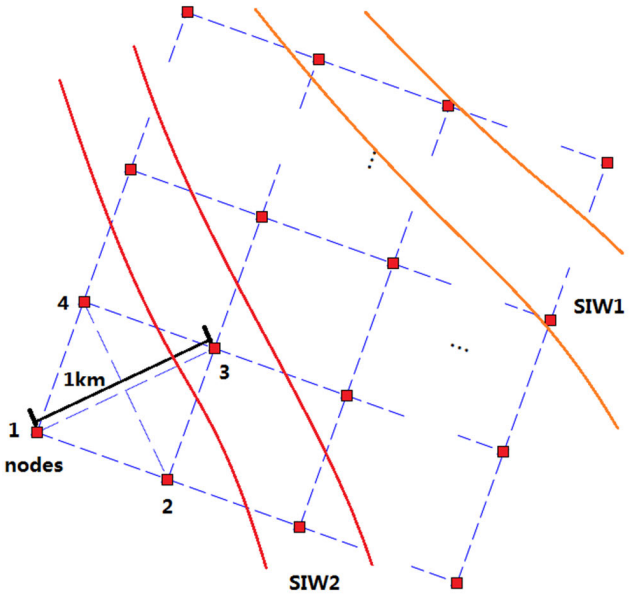

FIGURE 2. A sketch of node placement for distributed sensor network with passing SIWs.

fields are significantly perturbed and the various multi-path arrivals have a chance to interact with the SIWs. The SIWs of interest in this paper satisfy this condition, as described in Sec. III.A.

For one by one parameter estimation of individual solitons, the nodes (along the direction of SIWs propagation) must not be spaced too far so that the data are affected by only a single soliton. Large-scale monitoring for SIWs consisting of several solitons can be achieved by measuring acoustic data between nodes with longer spacing. An example of node placement for distributed sensor network are shown in Fig. 2, where the distances of node pairs deployed on diagonals of each small square mesh, like node pairs (1, 3) and (2, 4), are all set to 1 km.

The above concept of detection and parameter estimation of the SIWs using distributed sensors assume that the data can be transmitted into a central station for processing. This is not a problem if nodes are connected by cables to a power station. For remote nodes, data may need to be preprocessed at individual nodes and the reduced data will be transmitted to a central node assuming that underwater acoustic communications and networks have been set up and operational.

The specific methods of data processing are described in Sec. III.C – E.

III. SIMULATION ANALYSES

Simulated data are created in this section to evaluate the practicability of the proposed methods for future ocean experiments. Here we consider an environment in the northern SCS, where the existence of SIWs has been quite popular, and previously collected SSP data and buoyancy frequency can be used to simulate the acoustic field in the presence of SIWs.

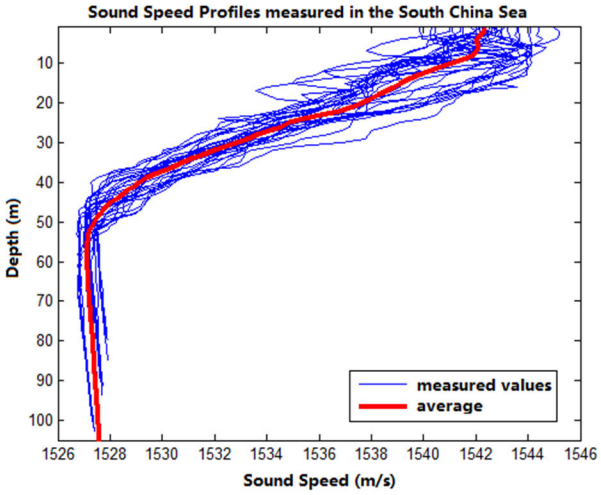

FIGURE 3. The SSP data measured in the northern South China Sea; the red line is the average.

A. OCEAN ENVIRONMENT AND SIW PROPERTIES

The simulation assumes an average water depth of 120 m. The SSP data came from an ocean experiment in May, 2016, where a total number of 39 sets of SSP data were measured in 6 days by a conductivity-temperature-depth (CTD) measuring instrument, as shown in Fig. 3. Those data exclude the effect of SIWs, and the corresponding average value of sound speed is 1530.5 m/s.

Many observations of SIWs in the northern SCS were reported [18]–[20], from which one can study the typical physical properties of SIWs in the area. The amplitude of solitons in this area is about 40 m [18]; it is much smaller than that of SIWs between Luzon Strait and Dongsha Islands (up to 170 m). The width of the solitons varies from hundreds of meters to more than 1 kilometer [19]. The width of a SIW packet composed of multiple solitons can reach up to several kilometers along its propagation direction, with intervals more than 10 kilometers between SIW packets [20]. The average propagation speed of SIWs is about 1.1 m/s [19].

Buoyancy frequency $N(z)$ determines the depth distribution of the SIWs or $H(z)$, and hence the sound speed perturbation induced by SIWs as given in (4). It can be measured using CTD. A set of buoyancy frequency data measured in the SCS [21] as well as corresponding values of $W(z)$ and $H(z)$ are shown in Fig. 4, where we assumed $G \sim 2.4\ \mathrm{s}^2/\mathrm{m}^2$ [12]. Figure 4 shows that the sound speed perturbation caused by SIWs is mostly notable at tens of meters below the surface, and can be observed even at depths of more than 100 m.

B. SIMULATION SETTINGS OF OCEAN ENVIRONMENT AND SIW PARAMETERS

A 3-dimensional acoustic environment is constructed for acoustic field simulation based on the oceanographic data of the northern SCS reported above. An average of SSP based on the experimental data is selected to be the reference SSP, as shown in Fig. 3. The reference sound speed is $c_0 = 1530.5$ m/s. For the bot-

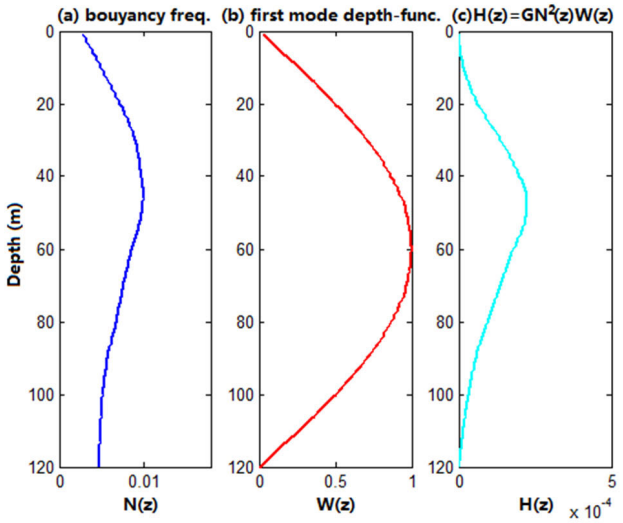

FIGURE 4. (a) Buoyance frequency data [21] and corresponding (b) first mode depth-function and (c) $H(z)$ in (4) of SIWs in the SCS.

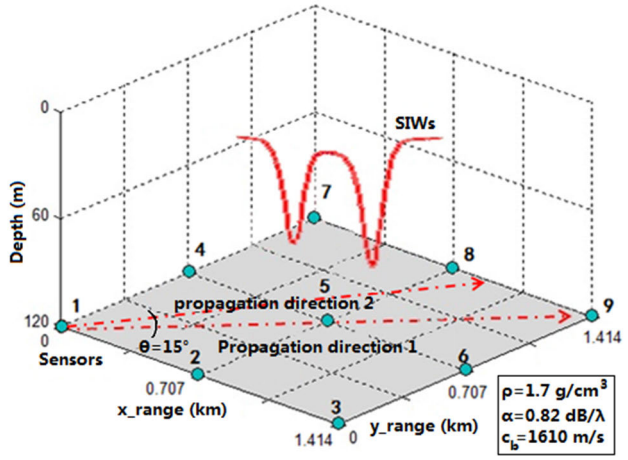

FIGURE 5. Illustration of simulation environment and SIW propagation.

tom, we assume a sound speed of $c_b = 1610$ m/s, density of $\rho = 1.7$ g/cm^3, and absorption coefficient $\alpha = 0.82$ dB/λ as shown in Fig. 5. For acoustic simulations, 9 distributed sensor nodes are deployed on the seabed at a depth of 119 m and form a square area with a radius of 2 km, as shown in Fig. 5. Each node can act as a transducer or a hydrophone in the simulation. Typical source level of 175 dB can be achieved for a transducer with a center frequency $f_c = 2$ kHz and bandwidth $Bw = 1$ kHz.

The 3-dimensional ocean model BELLHOP3D [22] is used in the simulation to generate accurate acoustic data, which can take the horizontal refraction of sound rays caused by SIWs into consideration, and thus has a better performance than 2-dimensional ocean model like RAM or BELLHOP. Here we just use the channel impulse responses (CIRs) as the acoustic data measured, generated by signal transmissions of 1kHz bandwidth and 2kHz center frequency, and the impulse response data are obtained by applying Inverse Fourier Transform (IFT) to sound pressures calculated by BELLHOP3D.

TABLE 1. Values of SIW parameters for the reference state.

Parameter	Meaning	Value
f_c	center frequency of acoustic signal	2 kHz
Bw	bandwidth of acoustic signal	1 kHz
η_1	amplitude of the first soliton	40 m
η_2	amplitude of the second soliton	37.5 m
Δ_1	characteristic width of first soliton	180 m
Δ_2	characteristic width of second soliton	200 m
L	interval between solitons	860 m
v	propagation speed of SIW	1 m/s
θ	propagation angle of SIW	0

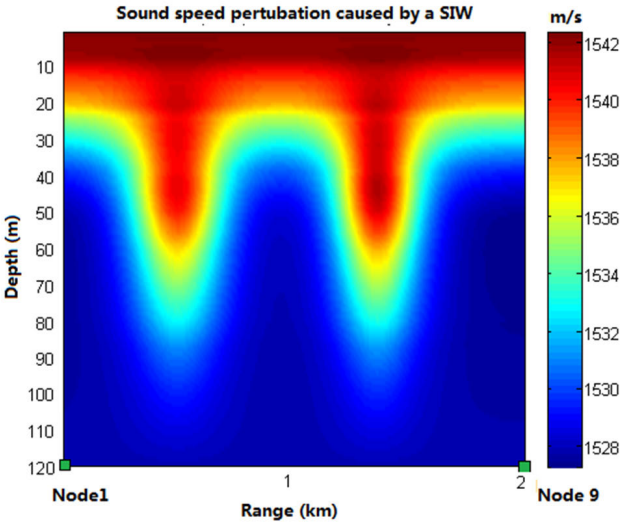

FIGURE 6. Illustration of sound speed perturbation caused by the SIW.

A model of SIWs is constructed based on (1) and (4), using the buoyancy frequency $N(z)$ and $H(z)$ shown in Fig. 4. The SIW packet contains two solitons moving along the direction from node 1 to node 9 as shown in Fig. 5. The SIW properties (parameters) are given in Table. 1. The propagation angle θ is defined as the angle between propagation direction of SIWs and the line through node 1 and node 9. For the SIWs propagating with $\theta = 0$ as shown in Fig. 5, the SSP along the vertical slice through node 1 and node 9 is shown in Fig. 6.

C. SIW DETECTION

1) CORRELATION OF CIRs WITH THE PASSAGE OF SIWs

We choose a small mesh consisted of node 1, 2, 4, and 5 shown in Fig. 5 for simulation analyses of SIW detection. As remarked in Sec. II.B, the pair of nodes $(2, 4)$ play an important role for the detection of the SIWs traveling from node 1 to node 5, as shown in the top panel of Fig. 7 for one of the solitons. The CIR from node 2 to node 4 is simulated as a function of time during the passage of a soliton. Selected CIRs are shown in the bottom panel of Fig. 7. The CIR in the absence of any SIW is used as the reference (denoted as "refer") and shown at the bottom. Other CIRs are shown for the soliton in different locations, labeled by the distance measured from the diagonal line (between node 2 and 4) of the mesh on the y-axis. One observes that the pulse arrival time and amplitudes change the most when the soliton is at

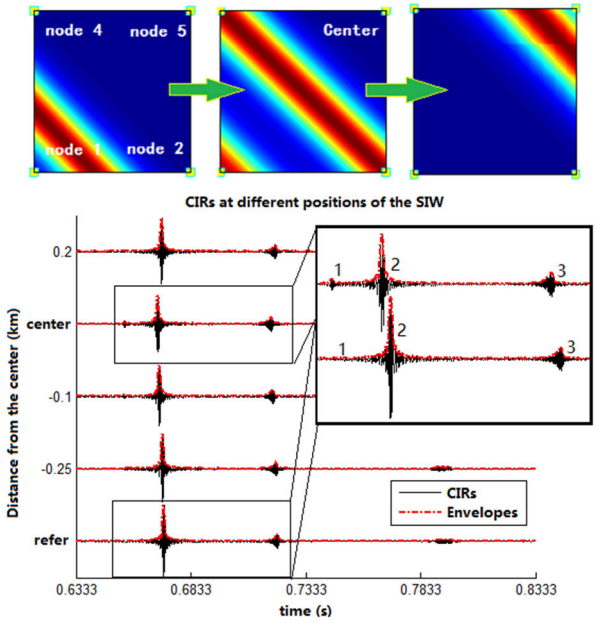

FIGURE 7. Top: display of a soliton (wave front) with respect to four nodes in a mesh. Bottom: CIRs between node 2 and 4 for the soliton at different positions, labeled by the distance from the center of the mesh on the *y*-axis. The CIR denoted by "refer" represents the data in the absence of the soliton.

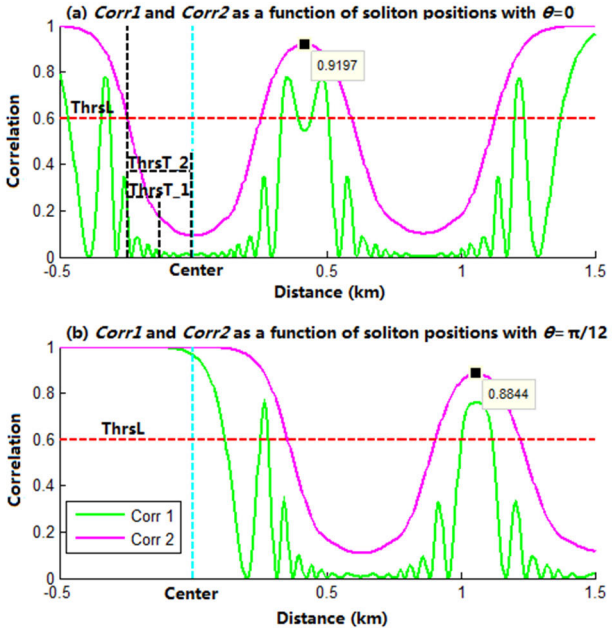

FIGURE 8. *Corr*1 and *Corr*2 as a function of the soliton positions when (a) $\theta = 0$ and (b) $\theta = \pi/12$. Thresholds *ThrsL* and *ThrsT* for SIW detection are also shown in this figure. Two minimums in (a) correspond to the passage of the first and second soliton in the SIW package.

the center position between node 1 and 5, marked by "center" on the *y*-axis. (For comparison with the "refer", the CIRs are enlarged shown in Fig. 7.) This is because the sound speed change reaches to the maximum at this position. One finds that the first pulse in the time series in Fig. 7 corresponds to the direct refracted ray arrival between node 2 and 4, and the second and third pulses correspond to rays reflected once and twice by sea surface, respectively.

The above simulated CIRs can be used to illustrate the performance of the detection algorithms using correlation coefficients *Corr*1 and *Corr*2 with the "refer" as the reference. The results are shown in Fig. 8(a). From Fig. 8(a) one finds that *Corr*1 and *Corr*2 are both sensitive to a soliton passing through. While *Corr*1 (correlation of CIRs) shows local fluctuations (due to signal phase change) with the moving soliton, we choose *Corr*2 (the correlation of envelops) to quantify the detection of a soliton (passing by). Two troughs in Fig. 8(a) represent the arrivals of the first and second solitons in the SIW wave packet, distinguished by the peak value of *Corr*2 between them.

In reality, the soliton wave front may not exactly align with node 2 and 4 as shown in the top panel of Fig. 7, as the propagation angle θ of the SIWs are changing with time, although staying in the general direction. (As stated above, θ as defined in Fig. 5 equals to 0 in Fig. 7.) The effect of the direction change is next simulated by changing θ from 0 to $\pi/12$. The results are in Fig. 8(b). One finds that the arrival of a soliton can also be detected using *Corr*2. The arrival time of the trough will shift based on the geometry and can be corrected after estimation of the arrival angle. See parameters estimation in Sec. III.D and III.E.

Two thresholds for *Corr*2 are used to quantify the detection performance. First, *Corr*2 has to be less than *ThrsL*, and second the time duration that $Corr2 < ThrsL$ has to be larger than *ThrsT*. The value of *ThrsL* may be chosen with experience, or based on constant false alarm rate (CFAR) condition as discussed below. For *ThrsT*, based on Fig. 8(a), one finds *Corr*2 is less than 0.6 for 0.5 km traveled by the soliton. Assuming that the soliton travels with $v = 1$ m/s, and then the time for $Corr2 < 0.6$ is about 500 s. *ThrsT* should then be set at half of that value [$\sim$ 4 min, *ThrsT*_2 in Fig. 8(a)] or less. In data processing, if the duration of the time when $Corr2 < ThrsL$ is longer than *ThrsT*, we decide that a soliton passes through the observation area.

2) DETECTION PERFORMANCE AND THE INFLUENCE OF THE NOISE

Monte Carlo simulations are used to verify the performance of the SIW detection approach. Assuming that the parameters of the soliton are random and uniformly distributed over the following windows: $\Delta \in [130, 230]$ m, $\theta \in [-\pi/6, \pi/6]$, and $v_{iw} = [0.8, 1.2]$ m/s, for each realization, we choose a random set of parameters to simulate the soliton passing through the simulation area, and use the proposed method to detect the existence of the soliton. Zero-mean Gaussian noises are added on measured acoustic data. For 500 times of detection simulations based on randomly generated values of parameters and with the signal-to-noise ratio $SNR = 0$ dB, the probability distribution of the detection (minimum value) of *Corr*2 is shown in Fig. 9(a), when SIWs are present versus the absence of SIWs. Here for a probability of false alarm $P_{fa} = 0.01$ for the case without a soliton

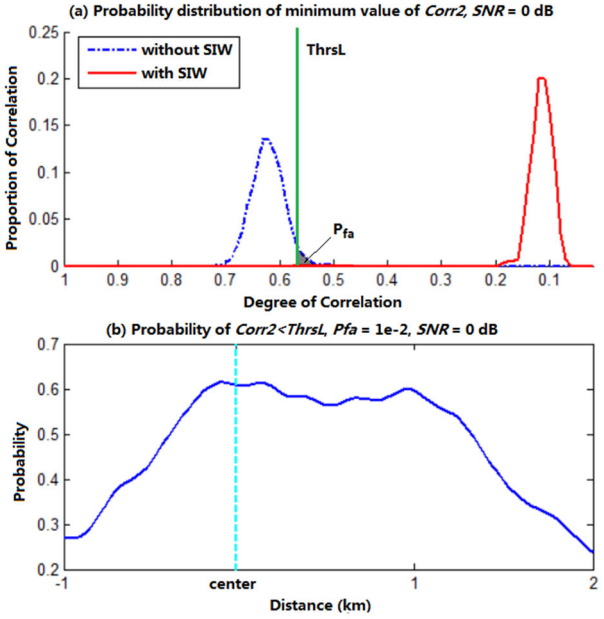

FIGURE 9. (a) Probability distribution of detection (minimum of *Corr*2) with and without SIWs within the mesh, and (b) Probability of *Corr*2 < *ThrsL* for different SIW positions for 500 times of detection simulations. Here CFAR P_{fa}= 0.01, *SNR* = 0 dB, $\Delta\in$ [130, 230]*m*, $\theta\in[-\pi/6,\pi/6]$, and v_{iw}= [0.8, 1.2]*m*/*s* for both (a) and (b).

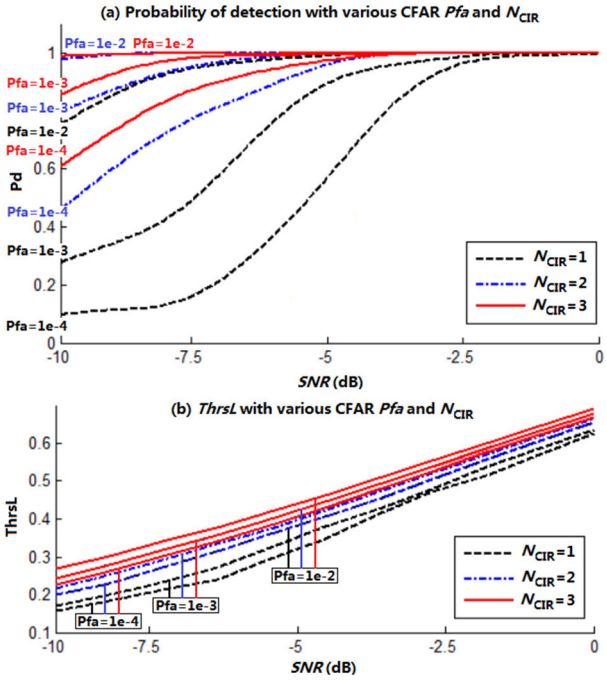

FIGURE 10. (a) CFAR detection performance and (b) the value of *ThrsL* with N_{CIR}= 1,2, and 3, and with various P_{fa}= $1e^{-4}$,$1e^{-3}$, and $1e^{-2}$.

(based on the shadow area under blue dash line), one finds $ThrsL = 0.5429$. Note that the probability distribution of detection of $Corr2$ is calculated by using the measurement values of $Corr2$ during the whole passage of SIWs. The probability of $Corr2 < ThrsL$, given a CFAR of $P_{fa} = 0.01$ for example, is shown in Fig. 9(b) for all measurement locations along the line of node 1 to 5 relative to the center position, with the parameters varying as given above and $SNR = 0$ dB. Fig. 9(b) implies that while a soliton with like $\theta = \pi/12$ may not be detected when it is at "center" position, it can be detected at the position of 0.5 km after "center", as shown in Fig. 8(b). In other words, Fig. 9(b) corresponds to a probability-based combination of Fig. 8(a) and Fig. 8(b) (and $Corr2$ with other values of θ), as a function of SIW positions. Note that both Fig. 9(a) and Fig. 9(b) are not the final probability of detection P_d, without consideration of $ThrsT$.

CFAR detection performance under different *SNRs* and $ThrsT$ are shown in Fig. 10(a) using the Monte Carlo method. With signal transmitted every minute, for $ThrsT = 1, 2,$ and 3 min, one has the number of continuous CIRs using for detection $N_{CIR} = 1, 2,$ and 3 respectively. The P_d for CFAR with $P_d = 1e^{-4}$, $1e^{-3}$, and $1e^{-2}$ is shown by the black dashed line for $N_{CIR} = 1$, blue dashed line for $N_{CIR} = 2$, and red solid line for $N_{CIR} = 3$ in Fig.10(a). As one can see from Fig. 10(a), for situations with relatively low *SNR* (e.g., −8 dB) and a constant value of P_{fa} (e.g., $1e^{-3}$), the detection performance using the dual-threshold detection method is significantly better than using the single-threshold one, and a reasonable larger value of $ThrsT$ may effectively improve P_d. This improvement of performance is mainly because $P_{fa,N_{CIR}=1}$ [i.e., the shadow area under blue dash line in Fig. 9(a)] increases (< 1) with increasing N_{CIR} as shown below [23]:

$$P_{fa,N=1} = (P_{fa})^{1/N_{CIR}}. \tag{9}$$

Thus, for CFAR with a given P_{fa}, the $ThrsL$ will increase with increasing N_{CIR} as shown in Fig. 10(b). Note that $ThrsL$ with different P_{fa} and $ThrsT$ may sometimes be overlapped according to (9), like $P_{fa} = 1e^{-2}$ and $N_{CIR} = 2$ versus $P_{fa} = 1e^{-3}$ and $N_{CIR} = 3$.

What's more, one also finds from Fig. 10(a) that for situations with *SNR* no less than about −4 dB, P_d of the dual-threshold detection method approaches 1 even with a relatively low value of P_{fa}; the proposed method is expected to work well. For *SNR* less than ~ -7 dB, as P_d decreases, the proposed method may have difficulties for effective detection. It is noted that for adjacent node pairs of distributed sensor network shown in Fig. 2, with a node distance of 1 km, the *SNR* of measured acoustic data is expected to be greater than 5 dB given a reasonable source level, e.g., 175 dB. In other words, the proposed method is expected to work well in real ocean environments.

3) THE INFLUENCE OF THE SOLITON AMPLITUDE

Next, we study the detection performance for solitons of different amplitudes. For $\eta_0 = 40$ m, Fig. 8(a) shows that the troughs of $Corr2$ as the solitons passing by can be used to confirm detection of solitons in the observation area. This applies to solitons with larger amplitudes. The question is the detection for solitons with smaller amplitudes. To answer this question, we plot in Fig. 11(a) that the $Corr2$ as a function

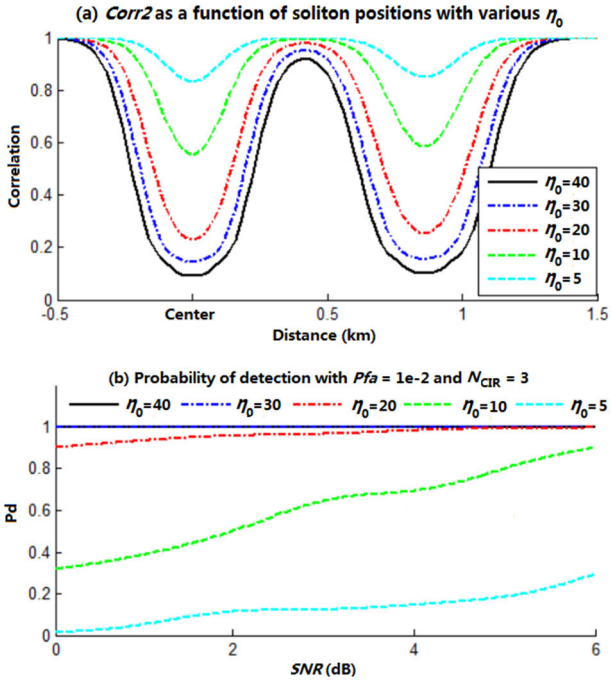

FIGURE 11. (a) *Corr*2 as a function of the soliton positions for various soliton amplitudes of η_0 in meters. (b) Probability of detection P_d for P_{fa}= 0.01 and N_{CIR}= 3.

of the soliton positions for values of η_0 varying from 40 m to 5 m. One finds the values of $Corr2$ for $\eta_0 \geq 20$ m still meet the detection criteria of the two thresholds mentioned above, whereas for smaller values of η_0, e.g., 10 m or 5 m, the values of $Corr2$ do not. The corresponding P_d is shown in Fig. 11(b) with $P_{fa} = 0.01$ and $N_{CIR} = 3$. Note that for cases with small values of η_0, one can possibly use a larger $ThrsL$ and a small value of $ThrsT$ (N_{CIR}) to improve the P_d at the expense of a larger P_{fa}. The choice of values is case dependent and will not be pursued here. Results imply that the proposed detection method may not work well with a very low η_0, especially under low-SNR situations.

D. SINGLE-PARAMETER ESTIMATION

With a proper design of node topology, one can ensure each mesh/grid of the node network contains no more than one soliton, then the properties of individual solitons (within the SIW package) can be studied one by one after the first soliton has been detected. For example, referring to Fig. 5 with $\theta = 0$, when the first soliton is detected by a node pair (2, 4), it is in the mesh surrounded by node 1, 2, 4, and 5, as shown in Fig. 12(a). When the first soliton is detected by node pair (6, 8), the first soliton is in the mesh surrounded by node 5, 6, 8, and 9, and the second soliton is in the mesh defined by node 1, 2, 4, and 5, as shown in Fig. 12(b). Consequently, the parameters of both solitons can be estimated one by one as illustrated below.

In this section, we use the MFI method, given in (8), to estimate the soliton parameters sequentially and iteratively. The five parameters to be estimated are: position r_0, characteristic width Δ_1, amplitude η_1, propagation angle θ of the

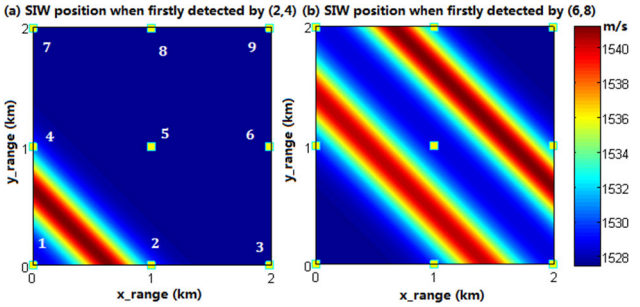

FIGURE 12. SIW positions when (a) node pair (2,4) and (b) node pair (6,8) firstly detects the presence of the SIW.

first soliton, and the interval L between solitons in the order specified. The data field of MFI method are CIRs measured from acoustic transmissions from node 1 to node 2, 4 and 5 and from node 2 to 4 for a soliton at r_0= 0.337 km, with $\Delta_1 = 186.97$ m, $\eta_1 = 38.78$ m, and $\theta = -\pi/16.36$. In the analyses below we use initial values for Δ_1, η_1, θ and L given in Table 1, based on the historical data.

1) ESTIMATION OF THE SOLITON POSITION

For estimating the position r_0, we assume that other parameters like Δ_1, η_1 and θ are fixed and given initially by the historical values in Table 1 in the first iteration, and later determined by previous estimation in the following iteration. Using the example discussed above, when the soliton moves along the direction from node 1 to node 9 in Fig. 5, the algorithm is designed to estimate r_0 as a function of time in post processing using data collected on node 1, 2, 4, and 5. For convenience, we draw a line from node 1 to 5, from 0.5 km before node 1 to 0.5 km after node 5. The location of the soliton is designated by the position referenced to the beginning of this line; 100 locations are selected uniformly separated by 20 m. For each soliton location, we calculate the CIRs from node 1 to node 2, 4 and 5 as well as from node 2 to 4 using BELLHOP3D (with the other soliton parameters fixed as mentioned above) and stored them as the replica field. The replica field is then correlated with the data field using (8). The position where the cost function B is maximum is the estimated position of the soliton.

In Fig. 13, we show, for example, the CIRs from node 1 to 2. The soliton position is denoted by the position displayed on the y-axis, where "refer" is the CIR in the absence of SIW. One observes in Fig. 13 the clear change in the CIRs as the soliton moves. This is the reason why node pair (1, 2) is included in the position estimation.

The result of position search is shown in Fig. 14(a), which plots the value of the cost function B as a function of search range for three cases of $SNRs$: $SNR = 10$, 5, and 0 dB. The data is from a soliton at position of $r_{0,real} = 0.337$ km, denoted as the true position. From the peak of the cost function, one estimates the position to be $r_{0,out} = 0.34$ km. The result shows that the cost function B is relatively sensitive to the change of SIW positions, and the estimated position matches well with the true value. In other words,

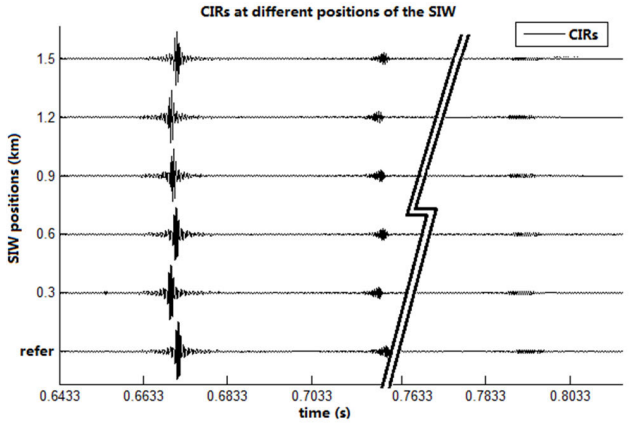

FIGURE 13. Change of CIRs with SIW position index of node pair (1, 2).

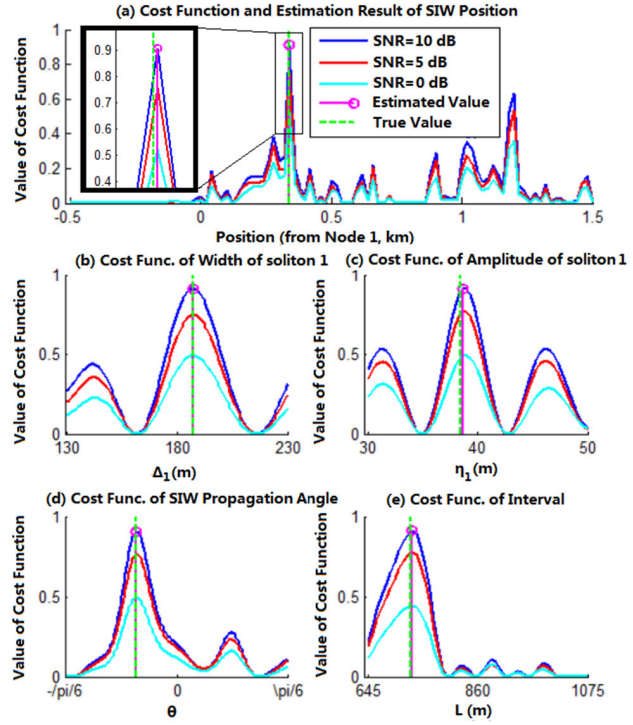

FIGURE 14. Cost function as a function of (a) soliton position, (b) soliton characteristic width, (c) soliton amplitude, (d) SIW propagation angle, and (e) interval between solitons. Ranges 0 and 1 correspond to positions of node 1 and 5.

the proposed method can effectively estimate the position of SIWs.

2) ESTIMATION OF THE CHARACTERISTIC WIDTH OF THE SOLITON

The same data, CIRs for a soliton at $r_0 = 0.337$ km, can be used to estimate the characteristic width of the soliton Δ_1. The soliton position r_0 has been estimated to be $r_{0,out} = 0.34$ km from III.C.1. For each value of Δ_1 changing from 130 m to 230 m, we calculate the CIRs in the same way as SIW position estimation (with η_1 and θ fixed as mentioned above) and stored them as the replica field. The replica field is next correlated with the data field using (8). The characteristic width where the cost function B is maximum is the estimated characteristic width of the soliton.

The result of characteristic width estimation is shown in Fig. 14(b) for $SNR = 10, 5$, and 0 dB. The data is generated for a soliton with characteristic width $\Delta_{1,real} = 186.97$ m. As shown in Fig. 14(b), the estimated characteristic width is $\Delta_{1,out} = 187$ m, which is matched with the real value of Δ_1. One can use the same method to estimate Δ_2 of the second soliton, based on the acoustic data collected when the second soliton enters the same mesh.

3) ESTIMATION OF THE SOLITON AMPLITUDE

The same data is next used to estimate the amplitude η_1 of the soliton. The soliton position r_0 and characteristic width Δ_1 have been previously estimated. For each value of η_1 varying from 30 m to 50 m, the replica field is calculated in the same way as SIW position estimation, and correlated with the data field using (8). The amplitude where the cost function B is maximum is the estimated amplitude of the soliton. The result is shown in Fig. 14(c). The true value is $\eta_{1,real} = 38.78$ m, and the estimation result is $\eta_{out} = 38.8$ m for all $SNR = 10$, 5, and 0 dB.

4) ESTIMATION OF THE SOLITON PROPAGATION ANGLE

After the value of r_0, Δ_1, and η_1 have been estimated, the same data and method are then applied to estimate the propagation angle θ, with searching value varying from $-\pi/6$ to $\pi/6$. The estimation result is shown in Fig. 14(d), where the true value is $\theta_{real} \approx -\pi/16.36$, and the estimated value is $\theta_{out} = -11\pi/180$ for all $SNR = 10$, 5, and 0 dB.

It can be seen from Fig. 14(b), (c), and (d) that the cost function B also has enough sensitivity for the parameters of Δ_1, η_1 and θ, thus one can obtain accurate estimation results by the proposed method. What's more, the above process can be repeated iteratively to improve the estimation. Iteration becomes important when the true values of SIW parameters are different from the historic values as assumed above. As long as the true values are not significantly different from the historical values, the iteration process is expected to converge.

5) ESTIMATION OF THE INTERVAL BETWEEN SOLITONS

Next, we estimate the interval L between two solitons. Because the historical value of the average propagation speed v of the SIW does not change much, the simplest method is that based on soliton detection as shown by $Corr2$ in Fig. 8(a), where the two troughs correspond to the arrival of the first and second soliton detected by nodes 2 and 4. Denoting time separation between the two troughs as τ, one finds $L = \tau v \cos\theta$. This allows an approximate estimation of L.

Another method of estimating L (which may be more precise) uses the MFI method given in (8). To achieve this goal, we need to use acoustic data measured over a larger area containing two solitons. For simulation analyses, we assume the geometry is as shown in Fig. 12(b). After the other parameters r_0, Δ_i, η_i, and θ have been determined, we can estimate the value of L from 645 to 1075 m by using the CIRs from

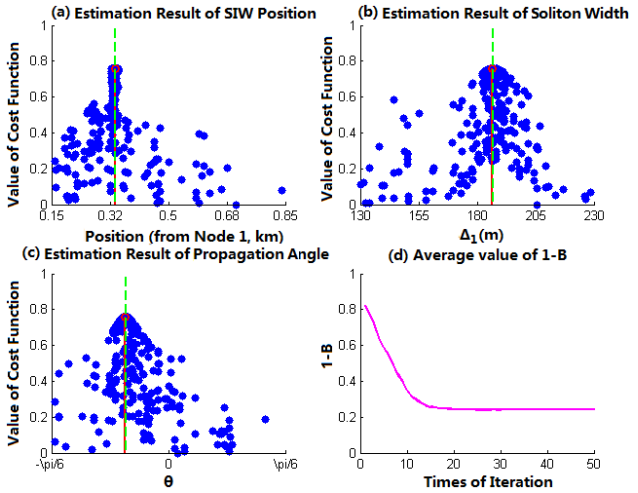

FIGURE 15. MFI results for multi-parameter integrated estimation of SIWs with $SNR = 5dB$. The red solid lines represent the estimation results, and the green dashed lines are the true values. (d) Values of $1 - B$ as a function of the number of iterations.

node 1 to node 3, 7, and 9. Matching the replica field with the data for $L_{real} = 729.06$ m, the cost function is shown in Fig. 14(e), yielding an estimated value of $L_{out} = 731$ m. The result shows that the proposed method also works well for this situation. After that, the average value of v can then be calculated more precisely as $v = L/(\tau \times \cos\theta)$.

Finally, one observes in Fig. 14 while the peak values of the cost function B decrease with decreasing SNR, the various parameters are still correctly estimated for SNR as low as 0 dB. This assumes that the iteration method converges so there is no significant mismatch (due to incorrect initial value) for any of the parameters. The lowest SNR required has to be determined from real data.

E. MULTI-PARAMETER ESTIMATION

Another approach to parameter estimation is to estimate the parameters of the SIW simultaneously using the inverse method, such as MFI. In this case, $\mathbf{x} = [r_0, \Delta_i, \theta]$ is a vector of parameters in (8), while η_i of each soliton is assumed to be known in advance for simplicity. The search for the maximum of the cost function B is a multi-dimensional search problem and requires a global optimization algorithm. Here, we use the Differential Evolution (DE) algorithm [24], which is one implementation of the genetic algorithm. To use the DE algorithm, one first needs to define the range of values for each parameter to be searched, as the result may vary depending on the window of search. The range of search used here is as follows: $r_0 = [0.15, 0.85]$ km from node 1, $\Delta_1 \in [130, 230]$ m, and $\theta \in [-\pi/6, \pi/6]$.

To run the DE algorithm, we use a population size $N_{DE} = 40$, mutation rate $CR = 0.7$, scaling factor of mutation $F = 0.8$, iteration times $= 80$, and $SNR = 5$ dB, then apply the algorithm to the same data as mentioned above with $r_{0,real} = 0.338$ km, $\Delta_{1,real} = 186.97$ m, and , $\theta_{real} \approx -\pi/16.36$. We show the scatter plots of the three parameters (marginal distributions) for one search during the DE iterations in Fig. 15. The mean values of the individuals in the last iteration are adopted as the final estimation results [red solid lines in Fig. 15(a)-(c)], where $r_{0,out} = 0.344$ km, $\Delta_{1,out} = 187.08$ m, and , $\theta_{out} \approx -\pi/16.72$; and the estimated parameters agree with the true values (greed dashed lines). Fig. 15 also displays the sensitivities of these parameters during the iterations, and shows that the DE algorithm is effective for multi-parameter estimation of the SIWs.

The interval between solitons L can be estimated after estimating the parameters of each soliton, as described in Sec. III.D. Similar with the single-parameter estimation method discussed in Sec. III.D, the multi-parameter estimation method also work well with a reasonable noise level, like $SNR = 5$ dB, which is easy to achieve given a reasonable source level like 175dB. A further idea is to estimate the parameters of multiple solitons r_0, η_i, Δ_i, θ, L, and v simultaneously using the acoustic tomographic method. This is workable in theory, but is computationally complex.

IV. SUMMARY AND DISCUSSION

In shallow water, the sound speed perturbation caused by SIWs can be modeled given SIW parameters assuming the conventional model for SIWs. Conversely, one can estimate the SIW parameters from the acoustic data using inverse methods. While direct observation of SIWs is possible using satellite and thermistor strings, they each have their own shortcomings as mentioned in the introduction. In this paper, we propose acoustic remote sensing methods using a distributed sensor network, which has a potential to provide wide area and full-time monitoring of the SIWs passing through the area. We developed a correlation-based method for detection of SIWs, as well as a time domain matching method for iterative sequential single parameter estimation and matched field inversion method for simultaneous multiple parameter inversion.

We conduct simulation analyses to validate the proposed methods. We use real oceanographic data collected in the northern South China Sea to study the feasibility of the proposed scheme, for future experimental planning. The simulation results show the methods can effectively detect the existence of SIWs and estimate SIW parameters, even under low signal-to-noise conditions or with relatively small amplitude of the soliton.

In real shallow water environments, other oceanographic related processes may also be present which may affect the detection and estimation of the SIWs as proposed, such as eddies, diffused internal waves, rough surfaces waves, fish school, etc. Except for the case of typhoons, these processes are expected to produce either a small perturbation on the CIRs or a change of CIRs on a time scale much slower than that induced by SIWs and will likely not significantly affect the proposed methods. See the Appendix for detailed discussions.

For practical applications, the iterative sequential single parameter search algorithm seems to be more suitable for in-buoy processing. It is only possible with distributed sensors.

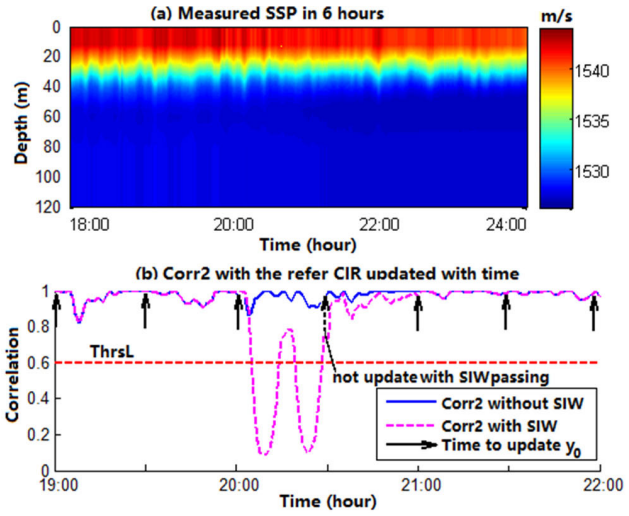

FIGURE 16. (a) The SSP data measured in the northern SCS using a CTD array from 18:00 to 24:00 in May 30, 2016. (b) *Corr*2 with and without the SIW when SSP changed and y_0 updated with time, the red dashed line is the typical value of *ThrsL*, and the arrows shows the time when y_0 is updated.

APPENDIX
EFFECTS OF OTHER OCEANOGRPAHIC RELATED PROCESSES ON THE PROPOSED METHODS

A. THE INFLUENCE OF THE CHANGES IN THE BACKGROUND SSP ON THE CIRs

Similar to SIWs, diffused internal waves may also be present in the shallow water, but the change in SSP induced by them are orders of magnitudes smaller compared with the SIWs. SSP in shallow water also changes with time on the scale of hours and longer time periods. An example of measured SSP data collected in the northern SCS on May 30, 2016 (before the SIWs arrived) from 18:00 to 24:00 is shown in Fig. 16(a) [25]. The data covered depth from 13m to 80m; that above 13 m and below 80m are extrapolated based on historical data. One observes the small and slow change of the SSP as discussed above. Many experiments [9], [10], [14] conducted in shallow water have shown that SIWs can be detected without being affected by these processes. We will use this data to show that the change of the correlation coefficient due to the SSP changes are small and will not pass the threshold for the detection of SIWs.

Assuming that the SSP between node 2 and 4 in Fig. 5 changes with time as shown in Fig. 16(a), we calculate the *Corr*2 as a function of time t based on (6), with $\mathbf{y}$ the measured CIR at t and $\mathbf{y}_0$ the reference CIR, which is the averaged CIR from measurements in the past 30 minutes (before the SIWs arrive). The result of *Corr*2 from 19:00 to 22:00 is shown by the blue solid line in Fig. 16(b), assuming that $\mathbf{y}_0$ is updated on the hour and on the half hour of each hour. In comparison, we next assume that a SIW consisted of two solitons passing through following the geometry shown in the top panel of Fig. 7, with physical properties (parameters) given in Table 1. By adding the SSP change due to the SIW on the SSP data in Fig. 16(a) based on (4), we calculate the *Corr*2 as a function of time, as shown by pink dashed line in Fig. 16(b). (One finds that the *Corr*2 is almost the same as that shown in Fig. 8 since SSP change due to the SIW is dominant. Note that $\mathbf{y}_0$ is not updated at 20:30 for the case with the SIW passing through.) As discussed in Sec. III.C (Fig. 8), a typical value of the first threshold *ThrsL* is 0.6, and SIWs are declared as present when $Corr2 < ThrsL$. The above results show that the small and slow changes in the SSP does not trigger the detection of the SIWs, i.e., $Corr2 > ThrsL$ because the amount of change in *Corr*2 is $\sim$ 0.2 or less. In contrast, the amount of change in *Corr*2 is on the order of 0.8 when the SIWs pass through, which is unmistakably large and will trigger the detection. Similar conclusions were drawn in a recent paper by Ren *et al.* in 2010 [26], in which the correlation is calculated using measured sound pressure data at 10 km from the source with and without SIWs present.

The above results can be understood because the fractional change in SSP is about 0.074% in the absence of SIWs compared with 0.446% in the presence of SIWs; the latter is about 6 times larger than the former. In addition, the changes in SSP due to SIWs extend much deeper into the water column and thus affect more the sound propagation.

B. THE INFLUENCE OF ROUGH SURFACE WAVES ON THE CIRs

Rough surfaces caused by tides, wind, etc. are random in time and space. They affect the sound propagation by reflecting/scattering the sound, causing attenuation and adding small perturbations to forwarding propagating sound [27]. The effect on the correlation of the CIRs, *Corr*2, can be illustrated using the BELLHOP3D model with a rough ocean surface option. Let the ocean surface be modeled as the superposition of several cosine waves [27], [28]:

$$\xi(r) = \sum_{n=1}^{N_{\cos}} a_n \cos(2\pi r/L_n + \varepsilon_n), \tag{10}$$

where $\xi(r)$ is the displacement of the ocean surface at range r, $N_{\cos}$ is the total number of cosine waves used, a_n, L_n, ε_n are the amplitude, wave length, and phase of the n-th cosine waves for $n = 1, 2, \cdots, N_{\cos}$, respectively. In the simulations to follow, we assume $N_{\cos} = 3, 4$ or 5 with $\varepsilon_n \sim \mathrm{U}(0, 2\pi)$ [27] and $L_n \sim \mathrm{U}(50, 150)$ m for each n in (10), where $\mathrm{U}(\cdot)$ represents the uniform distribution. The wave amplitude a_n is positive for each n, and obeys the Rayleigh distribution [28] with a scale parameter σ_a. We assume $\sigma_a = 0.46$ so that the averaged wave height (vertical distance between the peak and the trough) H_w of $\xi(r)$ is approximately equal to the annual averaged wave height in the northern SCS, as $H_w \approx 1.48$ m [29], [30]. A realization of the surface fluctuation $\xi(r)$ calculated from (10) between node 2 and 4 is shown in Fig. 17(a).

To estimate the change in *Corr*2 with and without surface waves, let $\mathbf{y}$ in (6) be the CIRs with surface waves, and $\mathbf{y}_0$ be that without surface waves. We assume the SSP between node 2 and 4 is constant and equal to the average value shown

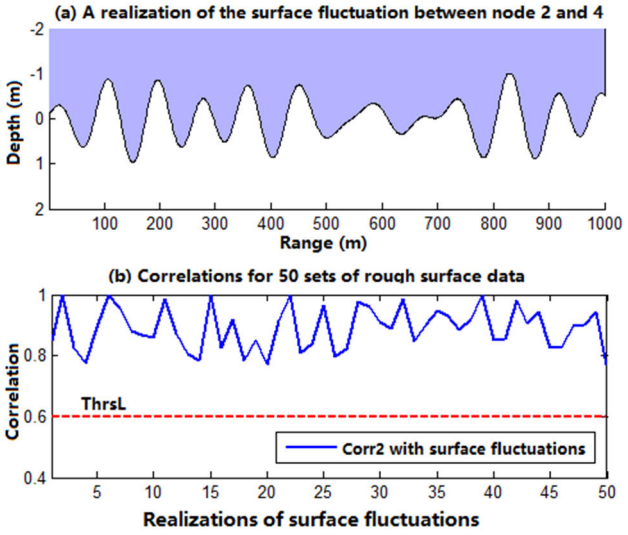

FIGURE 17. (a) A realization of the surface fluctuation between node 2 and 4. (b) *Corr*2 for 50 sets of randomly generated surface fluctuations.

in Fig. 3, then $\mathbf{y}_0$ without the passage of SIWs is the same with the "refer" state shown in Fig. 7, and the corresponding value of $Corr2$ is 0.925 for the surface fluctuation $\xi(r)$ shown in Fig. 13(a). We further generate 50 realizations of $\xi(r)$ with random values of $N_{\cos}$, a_n, L_n, and ε_n sampled from the distributions mentioned above. The calculated $Corr2$ in the presence of surface waves is shown in Fig. 17(b). One finds that $Corr2$ remains above 0.8 and is definitely larger than $ThrsL$ for each set of $\xi(r)$, implying that rough surface waves will likely not impact the performance of proposed methods for SIWs detection.

C. THE INFLUENCE OF FISH SCHOOLS ON CIRs

The passage of fish schools will cause the scattering of sound but their effects on $Corr2$ is small due to their small scattering strengths as reported in the literature. The sound pressure field P_{out} in the presence of a fish school can be expressed as [31]:

$$P_{out}(f) = P_{ori}(f) + P_{fish}(f) \tag{11}$$

where $P_{ori} = sG_{s,r}$ is the sound pressure without the fish school, $P_{fish} = sG_{s,fish}G_{fish,r}TS$ is the sound pressure scattered from the fish school, s is the source level, TS is the target strength of the fish school, $G_{s,r}$, $G_{s,fish}$, and $G_{fish,r}$ are the Green Function from the source to the receiver, from the source to the fish school, and from the fish school to the receiver, respectively, and f is the frequency. Feuillade *et al.* proposes a low-frequency acoustic scattering model for small fish schools in 1996 [32]. One finds from their work that the target strength TS is about -20 dB for a small group of 13 swimbladder-bearing fish at $\sim$ 2kHz. Coupled with two ways transmission loss from the source to the fish and then to the receiver, one finds that P_{fish} in (11) is $\sim$ 60 dB lower than P_{ori} for frequencies near 2 kHz. The corresponding change in CIRs due to the fish schools is minimal ($< 5\%$) and not expected to affect the detection of SIWs using the proposed method.

In summary, the above simulations "confirm" that the impacts of the passage of SIWs on the correlation of measured acoustic data, $Corr2$, is much larger than that caused by the random changes of SSP, (ordinary) rough surface waves, and the passage of fish schools, to allow detection of SIWs as previous experimental results have suggested.

ACKNOWLEDGMENT

The authors would specially thank to Dr. J. Li from the College of Information Science and Electronic Engineering, Zhejiang University, for providing the sound speed profile data measured in the northern SCS.

REFERENCES

[1] J. R. Apel, L. A. Ostrovsky, Y. A. Stepanyants, and J. F. Lynch, "Internal solitons in the ocean and their effect on underwater sound," *J. Acoust. Soc. Amer.*, vol. 121, no. 2, pp. 695–722, Feb. 2007.
[2] J. Zhou, X. Zhang, and P. H. Rogers, "Resonant interaction of sound wave with internal solitons in the coastal zone," *J. Acoust. Soc. Amer.*, vol. 90, no. 4, pp. 2042–2054, Oct. 1991.
[3] A. R. Osborne and T. L. Burch, "Internal solitons in the Andaman Sea," *Science*, vol. 208, no. 4443, pp. 451–460, May 1980.
[4] J. A. Shand, "Internal waves in the Georgia strait," *Eos Trans. Amer. Geophys. Union*, vol. 34, no. 6, pp. 849–856, 1953.
[5] W. Alpers, "Theory of radar imaging of internal waves," *Science*, vol. 314, no. 6008, pp. 245–247, 1985.
[6] K. Qu, F. Zhu, and W. Song, "A novel method for internal wave monitoring based on expansion of the sound speed profile," *Acta Oceanol. Sinica*, vol. 38, no. 4, pp. 187–193, 2019.
[7] T. F. Duda and J. C. Preisig, "A modeling study of acoustic propagation through moving shallow-water solitary wave packets," *IEEE J. Ocean. Eng.*, vol. 24, no. 1, pp. 16–32, Jan. 1999.
[8] T. F. Duda, "Acoustic mode coupling by nonlinear internal wave packets in a shelfbreak front area," *IEEE J. Ocean. Eng.*, vol. 29, no. 1, pp. 118–125, Jan. 2004.
[9] R. H. Headrick, J. F. Lynch, J. N. Kemp, A. E. Newhall, K. von der Heydt, J. Apel, M. Badiey, C.-S. Chiu, S. Finette, M. Orr, B. Pasewark, A. Turgot, S. Wolf, and D. Tielbuerger, "Acoustic normal mode fluctuation statistics in the 1995 SWARM internal wave scattering experiment," *J. Acoust. Soc. Amer.*, vol. 107, no. 1, pp. 201–220, Jan. 2000.
[10] R. H. Headrick, J. F. Lynch, J. N. Kemp, A. E. Newhall, K. von der Heydt, J. Apel, M. Badiey, C.-S. Chiu, S. Finette, M. Orr, B. Pasewark, A. Turgot, S. Wolf, and D. Tielbuerger, "Modeling mode arrivals in the 1995 SWARM experiment acoustic transmissions," *J. Acoust. Soc. Amer.*, vol. 107, no. 1, pp. 221–236, Jan. 2000.
[11] K. Yoo and T. C. Yang, "Broadband source localization in shallow water in the presence of internal waves," *J. Acoust. Soc. Amer.*, vol. 106, no. 6, pp. 3255–3269, Dec. 1999.
[12] T. C. Yang, "Acoustic mode coupling induced by nonlinear internal waves: Evaluation of the mode coupling matrices and applications," *J. Acoust. Soc. Amer.*, vol. 135, no. 2, pp. 610–625, Feb. 2014.
[13] D. Tielbürger, S. Finette, and S. Wolf, "Acoustic propagation through an internal wave field in a shallow water waveguide," *J. Acoust. Soc. Amer.*, vol. 101, no. 2, pp. 789–808, Feb. 1997.
[14] S. Finette, M. H. Orr, A. Turgut, J. Apel, M. Badiey, C.-C. Chiu, R. H. Headrick, J. N. Kemp, J. F. Lynch, A. E. Newhall, K. Heydt, B. Pasewark, S. N. Wolf, and D. Tielbuerger, "Acoustic field variability induced by time evolving internal wave fields," *J. Acoust. Soc. Amer.*, vol. 108, no. 3, pp. 957–972, 2000.
[15] S. Finette and R. Oba, "Horizontal array beamforming in an azimuthally anisotropic internal wave field," *J. Acoust. Soc. Amer.*, vol. 114, no. 1, pp. 131–144, Jul. 2003.
[16] A. Tolstoy, *Matched Field Processing for Underwater Acoustics*, vol. 1. Singapore: World Scientific, 1993.
[17] J. Luo, M. Badiey, E. A. Karjadi, B. Katsnelson, A. Tskhoidze, J. F. Lynch, and J. N. Moum, "Observation of sound focusing and defocusing due to propagating nonlinear internal waves," *J. Acoust. Soc. Amer.*, vol. 124, no. 3, pp. 66–72, 2008.

[18] Z. Xu, B. Yin, Y. Hou, Z. Fan, and A. K. Liu, "A study of internal solitary waves observed on the continental shelf in the northwestern South China Sea," *Acta Oceanol. Sinica*, vol. 29, no. 3, pp. 18–25, May 2010.
[19] M. H. Orr, "Nonlinear internal waves in the South China Sea: Observation of the conversion of depression internal waves to elevation internal waves," *J. Geophys. Res.*, vol. 108, no. C3, pp. 1–16, 2003.
[20] M.-K. Hsu and A. K. Liu, "Nonlinear internal waves in the South China Sea," *Can. J. Remote Sens.*, vol. 26, no. 2, pp. 72–81, Apr. 2000.
[21] T. Hu and T. Gao, "An expression of internal wave vertical modes equation in some shallow waters," *Acta Oceanol. Sinica*, vol. 29, no. 4, pp. 148–151, 2007.
[22] M. B. Porter, "Out-of-plane effects in three-dimensional oceans," *J. Acoust. Soc. Amer.*, vol. 137, no. 4, p. 2419, 2015.
[23] S. M. Kay, *Fundamentals of Statistical Signal Processing*. Upper Saddle River, NJ, USA: Prentice-Hall, 1998.
[24] R. Storn and K. Price, "Differential evolution—A simple and efficient heuristic for global optimization over continuous spaces," *J. Global Optim.*, vol. 11, no. 4, pp. 341–359, 1997.
[25] J. Li, private communication, 2016.
[26] Y. Ren and Z. Li, "Effects of internal waves on signal temporal correlation length in the South China Sea," *Chin. J. Oceanol. Limnol.*, vol. 28, no. 5, pp. 1119–1126, Sep. 2010.
[27] J. R. Daugherty and J. F. Lynch, "Surface wave, internal wave, and source motion effects on matched field processing in a shallow water waveguide," *J. Acoust. Soc. Amer.*, vol. 87, no. 6, pp. 2503–2526, Jun. 1990.
[28] C. C. Tung and N. E. Huang, "Covariances and spectra of the kinematics and dynamics of nonlinear waves," *J. Geophys. Res.*, vol. 90, no. C6, pp. 11911–11916, 1985.
[29] Y. Q. Qu, P. Shi, and Q. W. Mao, "Characteristics of sea wave over the northern South China Sea from GEOSAT altimetric observations," *Acta Oceanol. Sinica*, vol. 20, no. 2, pp. 20–26, 1998.
[30] L. Wu, X. L. Wang, and Y. Feng, "Historical wave height trends in the South and East China Seas, 1911–2010," *J. Geophys. Res., Oceans*, vol. 119, no. 7, pp. 4399–4409, Jul. 2014.
[31] P. Ratilal, Y. Lai, and N. C. Makris, "Validity of the sonar equation and Babinet's principle for scattering in a stratified medium," *J. Acoust. Soc. Amer.*, vol. 112, no. 5, pp. 1797–1816, Nov. 2002.
[32] C. Feuillade, R. W. Nero, and R. H. Love, "A low-frequency acoustic scattering model for small schools of fish," *J. Acoust. Soc. Amer.*, vol. 196, no. 1, pp. 196–208, 1996.
[33] M. Ouimet and J. Cortes, "Collective estimation of ocean nonlinear internal waves using robotic underwater drifters," *IEEE Access*, vol. 1, pp. 418–427, 2013.

TONGCHEN WANG received the B.S. degree in information and communication engineering from Zhejiang University, Hangzhou, China, in 2013, where he is currently pursuing the Ph.D. degree in marine remote sensing with the College of Information Science and Electronic Engineering.

From 2014 to 2015, he was a Research Assistant with the Institute of Signal Space and Information System, Zhejiang University. His research interests include marine remote sensing, ocean acoustic tomography, acoustic signal processing, and parameter estimation of solitary internal waves.

T. C. YANG received the Ph.D. degree in high energy physics from the University of Rochester, Rochester, NY, USA, in 1971.

From 2012 to 2014, he was a National Science Counsel Chair Professor with National Sun Yat-sen University, Kaohsiung, Taiwan. Before that, he spent 32 years working at the Naval Research Laboratory, Washington, DC, serving as the Head of the Arctic Section, Dispersive Wave Guide Effects Group, and acting Head of the Acoustic Signal Processing Branch, and consultant to the division on research proposals. He is currently a Professor and previously a Pao Yu-Kong Chair Professor with Zhejiang University. His current research focuses on array signal processing exploring super-directivity and super-gain and applications, environmental acoustic sensing and signal processing using distributed networked sensors, and methods for improved channel tracking and data-based source localization. In earlier years, he pioneered matched mode processing for a vertical line array, and matched-beam processing for a horizontal line array. Other areas of research include underwater acoustic communications, geoacoustic inversions, waveguide invariants, effects of internal waves on sound propagation in shallow water, and arctic acoustics.

Dr. Yang is a Fellow of the Acoustical Society of America.

WEN XU (Senior Member, IEEE) received the B.E. degree in electrical engineering from the University of Science and Technology of China, Hefei, China, in 1990, the M.S. degree in acoustics from the Institute of Acoustics, Chinese Academy of Sciences, Beijing, China, in 1993, and the Ph.D. degree in oceanographic engineering from the Massachusetts Institute of Technology (MIT), Cambridge, MA, USA, jointly with Woods Hole Oceanographic Institution, Woods Hole, MA. USA, in 2001.

From 1993 to 1996, he was a Research Engineer with the Institute of Acoustics, Chinese Academy of Sciences. He was with the Ocean Acoustics Group, MIT, as a Research Scientist, from 2001 to 2002, and with the Teledyne RD Instruments, San Diego, CA, USA, as a Research Scientist/Senior Research Scientist, from 2003 to 2007. He is currently a Professor with the Ocean College and College of Information Science and Electronic Engineering, Zhejiang University, Hangzhou, China. His research has concerned statistical and array signal processing in general and in applications to sonar, radar, and communication systems, and most recently to underwater sensor networks.

Dr. Xu has been an Associate Editor of the IEEE JOURNAL OF OCEANIC ENGINEERING, since 2010.